Clinical, Cosmetic and Investigational Dermatology

Dovepress
Taylor & Francis Group

Open Access Full Text Article

ORIGINAL RESEARCH

Integrated Transcriptomic and Single-Cell Analyses Link ATP7A, a Cuproptosis-Related Hub Gene, to ECM-Adhesion Signaling Dysfunction in UVB-Induced Skin Photodamage

Shiyang Li[1,2], Wei Wan[3], Ting Meng[1,2], Jie Zhang[1,2], Yu Xiao[1,2], Xianwei Cao[1,2]

[1]Department of Dermatology, The First Affiliated Hospital, Jiangxi Medical College, Nanchang University, Nanchang, People's Republic of China; [2]Institute of Dermatology, Jiangxi Academy of Clinical Medical Sciences, Nanchang, Jiangxi, People's Republic of China; [3]Department of Critical Care Medicine, The First Affiliated Hospital, Jiangxi Medical College, Nanchang University, Nanchang, People's Republic of China

Correspondence: Xianwei Cao; Yu Xiao, Department of Dermatology, The First Affiliated Hospital of Nanchang University, Nanchang, Jiangxi, People's Republic of China, Email ndyfy00050@ncu.edu.cn; yyyxy09@163.com

Objective: To investigate the link between UVB-induced skin photodamage and cuproptosis, and identify key regulatory genes.

Methods: Transcriptomic data from UVB-irradiated human skin (GSE41078) were obtained from GEO. Differentially expressed genes (DEGs) were identified, followed by GO and KEGG enrichment, and WGCNA. Key regulators were defined by intersecting DEGs, cuproptosis-related genes (CRGs), and the WGCNA module most correlated with photodamage. Single-cell RNA-seq data (GSE289389) were used to assess ATP7A expression in keratinocytes and to infer cell–cell communication (CellChat), focusing on ECM and adhesion signaling. Hub genes were validated via qRT-PCR and Western blot in UVB-induced acute photodamage cells and mouse models.

Results: Examination of the GSE41078 dataset revealed 509 DEGs associated with photodamage. WGCNA identified the blue module as most strongly correlated with photodamage. Cross-referencing 978 core module genes with 55 CRGs and 509 DEGs identified a single hub gene, ATPase copper transporting alpha (ATP7A). Single-cell analysis confirmed significant ATP7A downregulation after UVB exposure ($p = 1.83 \times 10^{-5}$) and showed that ATP7A-high keratinocytes exhibited stronger integration with stromal cells via enhanced ECM–adhesion signaling (e.g. collagen, laminin), whereas ATP7A-low cells displayed weakened responsiveness to microenvironmental cues. Experimental confirmation suggested that both mRNA and protein expression of ATP7A were markedly diminished in photodamaged cellular and mouse models ($P < 0.05$), aligning with the computational predictions.

Conclusion: This study suggests a potential association between ATP7A downregulation and UVB-induced photodamage with possible relevance to cuproptosis-related pathways. ATP7A downregulation is associated with reduced ECM-adhesion signaling interactions in keratinocytes, as indicated by CellChat. This analysis provides new clues to the mechanism of photodamage and suggests that ATP7A may be involved in the functional regulation of skin photodamage.

Keywords: UVB, skin photodamage, cuproptosis, ATP7A, bioinformatics analysis

Introduction

Skin constitutes the most extensive organ within the human body and functions as the foremost defensive barrier against environmental insults, encompassing microorganisms, chemical agents, airborne pollutants, and, most notably, solar ultraviolet (UV) radiation.[1,2] Ultraviolet radiation is categorized into ultraviolet A, ultraviolet B (UVB), and ultraviolet C according to wavelength. Among these, UVB exhibits limited penetration depth and is predominantly absorbed by the epidermis (70%) and superficial dermis (10%).[3] Therefore, UVB is regarded as a major exogenous contributor to skin photodamage.[4] Sustained UVB irradiation provokes cumulative skin injury and accelerates aging, while also driving the initiation of photo-induced cutaneous malignancies like squamous cell carcinoma, basal cell carcinoma, and melanoma.[5]

https://doi.org/10.2147/CCID.S607933
Received: 12 March 2026
Accepted: 4 June 2026
Published: 15 June 2026

Experimental evidence indicates that prolonged or excessive UVB exposure elicits overproduction of reactive oxygen species (ROS) within the epidermis, thereby activating diverse oxidative stress signaling cascades, encompassing the nuclear factor kappa B (NF-κB) and mitogen-activated protein kinase pathways.[6,7] These alterations precipitate lipid and protein peroxidation, mitochondrial and DNA impairment, disruption of membrane permeability, cell cycle arrest, and extracellular matrix degradation, culminating in skin tissue damage.[8] Importantly, mitochondria are a primary target of UVB-induced oxidative stress. UVB irradiation causes mitochondrial dysfunction, including loss of membrane potential, reduced ATP synthesis, and impaired mitophagy.[9,10] Recent investigations have further demonstrated that various molecular mechanisms contribute to photodamage,including apoptosis,[6] autophagy,[11] and ferroptosis.[12]

Cuproptosis, first described by Tsvetkov et al in 2022,[13] represents a distinct programmed cell death modality triggered by intracellular copper accumulation and is also intrinsically linked to mitochondrial stress. This process involves abnormal copper attachment to lipoylated proteins in the tricarboxylic acid cycle, which initiates oligomerization of mitochondrial lipoylated proteins and decreases iron-sulfur (Fe-S) cluster proteins, thereby inducing proteotoxic stress that ultimately results in cell death.[14] The morphological hallmarks of cuproptosis include mitochondrial contraction, rupture of the plasma membrane, endoplasmic reticulum injury, and chromatin fragmentation. Thus, UVB-induced photodamage and cuproptosis converge on mitochondrial dysfunction: UVB damages mitochondria through oxidative attack, whereas cuproptosis stresses mitochondria via copper-driven proteotoxic stress. Based on this, We hypothesize that UVB-induced oxidative stress impairs copper-exporting ATPases, leading to aberrant accumulation of intracellular Cu^{+}. The accumulated Cu^{+} then amplifies ROS production via Fenton-like reactions,[15] thereby damaging mitochondrial function.Currently, extensive investigations have focused on its involvement in neurodegenerative disorders, cardiovascular diseases, and malignancies.[16–18] However, studies investigating the relationship between cuproptosis and UVB-induced skin photodamage remain limited.

Therefore,gene chip datasets of UVB-induced photodamaged skin were procured from the Gene Expression Omnibus (GEO) database, and bioinformatics strategies were applied to identify genes linked to both photodamage and cuproptosis, which were subsequently validated in cellular and mouse photodamage models. This investigation was designed to elucidate the role of cuproptosis in UVB-mediated skin photodamage, determine its activation status under photodamage conditions and recognize hub genes regulating this process, thereby introducing a novel "copper ion" perspective for comprehending skin photodamage and suggesting potential biomarkers and therapeutic targets for interventions in skin injury and aging.

Materials and Methods

Bioinformatics Analysis Methods

Gene Expression Microarray Data and Cuproptosis Data Sources

Gene expression profiles associated with UVB-induced photodamage were procured from the GEO database of the National Center for Biotechnology Information (https://www.ncbi.nlm.nih.gov/geo/). The search strategy employed the keywords "(UVB) AND (Homo sapiens)", and datasets were screened based on the following eligibility standards. The criteria were defined as follows: (1) datasets must consist of mRNA transcriptome gene matrices; (2) data must originate from human skin tissue subjected to UVB irradiation; (3) both expression profiling and high-throughput sequencing approaches were acceptable; (4) datasets were required to include comparative analyses of gene chip expression between healthy controls and lesional skin of patients experiencing acute photodamage; and (5) the overall sample size had to be no fewer than 20. Datasets that failed to satisfy these requirements were excluded. After applying these filters, one qualifying dataset (GSE41078) was identified within GEO. Gene set IDs from GSE41078 were subsequently mapped to gene symbols using Perl scripts. DEGs were subsequently characterized using Gene Ontology (GO) and Kyoto Encyclopedia of Genes and Genomes (KEGG) pathway analyses, functional enrichment, and weighted gene co-expression network analysis (WGCNA). Furthermore, 55 cuproptosis-related genes (CRGs) were procured from the Genecards database (www.genecards.org/) by searching the keyword "cuproptosis". Key regulators were identified by intersecting DEGs, CRGs, and genes within the WGCNA module exhibiting the strongest correlation with the

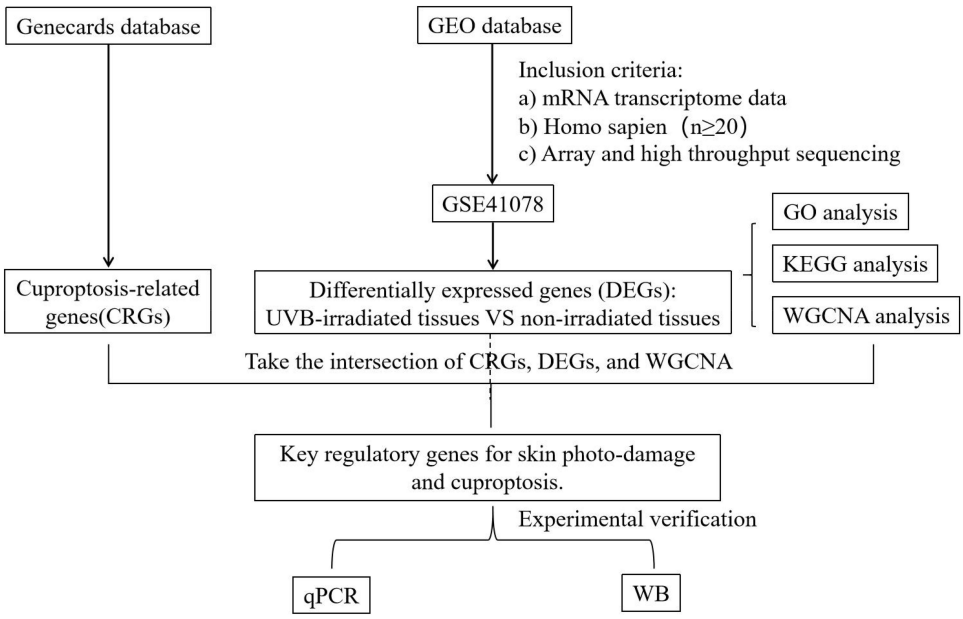

Figure 1 Flowchart of the study.

photodamage phenotype. Validation of hub genes was performed in UVB-induced acute photodamage cells and mouse models through quantitative real-time polymerase chain reaction (qRT-PCR) and Western blot (WB) assays.(Figure 1).

Microarray Data Preprocessing and Differentially Expressed Genes Screening

Differential expression of mRNAs in the GSE41078 dataset, comparing photodamaged and normal skin tissues, was analyzed with the "limma" package in R4.0.3. Prior to analysis, normalization of the dataset was carried out using the "limma" package. Two-tailed Student's t-tests were applied to compute individual *P*-values. The criteria for identifying DEGs were set as adjusted $P < 0.05$ and $|\log_2$ fold change (FC)$| > 1.5$. Genes exhibiting logFC > 1.5 were deemed upregulated, while those displaying logFC < −1.5 were categorized as downregulated. DEGs associated with UVB-induced photodamage were further extracted based on *P*-values < 0.05. Visualization of the differential expression results was conducted through volcano plots and heatmaps generated with the pheatmap and ggplot packages.

Functional Analysis and Enrichment Analysis of DEGs

Gene Ontology enrichment analysis[19] and Kyoto Encyclopedia of Genes and Genomes pathway analysis[20] were applied to DEGs to clarify their major biological roles and pathway participation. Functional characterization of DEGs within signaling pathways was conducted using the clusterProfiler package[21] together with the enrichplot package in R software. Visualization of the enrichment outcomes was carried out with the ggplot2 package.

Weighted Gene Co-Expression Network Analysis and Co-Expression Gene Modules Closely Related to Photodamage

To examine the association between gene expression and clinically relevant phenotypes, WGCNA was conducted to detect co-expression modules. Using the WGCNA package, genes within the top 25% variance of the dataset (4,018 genes) were selected for subsequent analysis. The analytical parameters were defined as cutHeight = 65 and soft threshold = 12. The weighted adjacency matrix was converted into a topological overlap matrix (TOM) to assess network connectivity, followed by hierarchical clustering to construct the TOM-based dendrogram, where modules were differentiated through distinct color coding. Subsequently, Pearson correlation analysis was executed to identify relationships between gene modules and clinical characteristics, with the module exhibiting the highest correlation coefficient being selected for additional investigation. Key genes linked to photodamage were identified by intersecting the core

genes from the most positively correlated WGCNA module with both DEGs and CRGs, followed by visualization through a Venn diagram.

Identification and Communication Analysis of Keratinocyte Subpopulations Based on ATP7A Expression

Single-cell RNA-seq data were obtained from the Gene Expression Omnibus (GEO; accession number GSE289389) and analyzed using Seurat. Raw count matrices were used to construct Seurat objects. Genes detected in fewer than 3 cells and cells with fewer than 200 detected genes were removed during object construction. After merging individual samples, cells were further filtered using the following quality control criteria: $1,000 \leq$ nCount_RNA $\leq 50,000$, $200 \leq$ nFeature_RNA $\leq 6,000$, and mitochondrial gene percentage $\leq 15\%$. After quality control, 34,856 cells were retained, including 17,581 Control cells and 17,275 UVB cells.Gene expression was normalized using LogNormalize with a scale factor of 10,000. The top 2,000 highly variable genes were identified using the variance-stabilizing transformation method. Cell-cycle scores were calculated using Seurat cell-cycle gene sets, and S-phase and G2/M-phase scores were regressed out during data scaling. PCA was performed based on highly variable genes. When batch correction was required, Harmony was applied using sample identity as the batch variable. Principal components were evaluated using PC heatmaps, JackStraw analysis with 100 replicates, and ElbowPlot. A shared nearest-neighbor graph was constructed using the first 9 principal components, and Louvain clustering was performed. Multiple resolutions were assessed using clustree, and a final resolution of 0.1 was selected. UMAP and t-SNE were generated using the first 10 principal components.Marker genes were identified using FindAllMarkers with only.pos = TRUE, min.pct = 0.25, and logfc.threshold = 0.25. Cell types were annotated using SingleR and canonical marker genes. A total of 14,142 keratinocytes were identified, including 5,582 Control and 8,560 UVB keratinocytes. ATP7A expression was compared between groups and visualized on UMAP. Keratinocytes were divided into ATP7A high and ATP7A low groups by median ATP7A expression. Cell-cell communication was inferred using CellChat with the human ligand-receptor database, excluding groups with fewer than 10 cells. Global networks, signaling pathways, and ligand-receptor pairs were analyzed, focusing on extracellular matrix- and adhesion-related signaling.

Materials and Methods for in vitro Experimental Validation

Hub genes were identified through bioinformatics analysis, and subsequent in vitro validation experiments were carried out to strengthen the reliability of the research results.

Cell Culture

HaCaT cell line was supplied by the Cell Bank of the First Affiliated Hospital of Nanchang University (China).The human keratinocyte cell line (HaCaT) was maintained in DMEM comprising 10% fetal bovine serum (Servicebio, China) and 1% penicillin-streptomycin. Cultures were maintained in a tri-gas chamber at 37 °C with 5% CO_2. Subculturing was performed once cell confluence reached approximately 80%, and cells in the logarithmic growth phase were subsequently utilized for experimental procedures.

Establishment of the Acute Photodamage Cell Model

The HaCaT cell UVB-induced photodamage model was established with reference to the protocol of KUNCHANA et al[22] incorporating minor modifications.HaCaT cells were placed at suitable densities in 6-cm culture plates and maintained at 37 °C under 5% CO_2 conditions for 24 h. When cultures reached 70–80% confluence, the modeling procedure was initiated. Cells were split into two groups: a control group and a UVB group. Before irradiation, a thin layer of phosphate-buffered saline (PBS) was applied to cover the cells, followed by UVB exposure using a lamp (Nanchang University LED Center, 310–312 nm) at a dose of 40 mJ/cm^2, measured by Linshang Technology Co., Ltd. (Shenzhen, Guangzhou, China). After exposure, PBS was replaced with DMEM comprising serum, and cells underwent cultivation for a further 24 h. Control cultures underwent the same treatment protocol except for UVB irradiation.

Animal Culture

Six male BALB/c mice, aged 4~6 weeks with an average body weight of approximately 18 g, were procured from Jiangsu Jicui Yaokang Biotechnology Co., Ltd. (Certificate:SCXK20230009). The animals were kept in the specific

pathogen-free animal facility at the First Affiliated Hospital of Nanchang University (Animal Ethics:CDYFY-IACUC -202410GR017), provided with standard chow and water ad libitum, and given a 7-day acclimatization period prior to experimental procedures. All animal-related procedures were executed per the *Experimental Animal License Management Regulations* and the *Laboratory Animal Management Regulations* of the First Affiliated Hospital of Nanchang University.Mice were anesthetized in a chamber containing 2% isoflurane in oxygen and maintained using a face mask with isoflurane. The mice were euthanized by cervical dislocation.

Establishment of an Acute Photodamage Animal Model

The mouse photodamage model was established as described previously,[23] Before modeling, the dorsal skin of each mouse was shaved with a razor and subsequently depilated twice using depilatory cream. Six mice designated for modeling were arbitrarily split into two groups: a control group and a UVB group, with three animals in each. UVB exposure was administered using a phototherapy device placed in a dark environment, with an irradiation distance of 6 cm, an intensity of 1 mJ/(cm^2·s), and a single cumulative dose of 200 mJ/cm^2. Irradiation was applied continuously for 3 consecutive days, after which morphological and histological alterations of the dorsal skin were assessed. Control animals underwent the same procedure without UVB irradiation.

Hematoxylin and Eosin Staining of Mouse Skin Tissue

Mouse skin tissues underwent fixation in 10% neutral formalin for 24 h, succeeded by automated dehydration and paraffin embedding. The embedded specimens were sectioned using a rotary microtome and subsequently deparaffinized in water. Hematoxylin and eosin (H&E) staining was performed according to the following protocol: hematoxylin staining for 10–20 min; rinsing with tap water for 1–3 min; differentiation using acid alcohol for 5–10 s; rinsing with tap water for 1–3 min; bluing in 50 °C warm water or weak alkaline solution until blue coloration developed; rinsing with tap water for 1–3 min; 85% ethanol treatment for 3–5 min; eosin staining for 3–5 min; rinsing with water for 3–5 s; graded ethanol dehydration; xylene clearing; and mounting using neutral balsam. Following microscopic observation, the stained slides underwent digital scanning.

Validation of Inflammatory Factors and ATP7A in Cell and Animal Models

For qRT-PCR, total RNA was procured from UVB-exposed cells and animal tissues employing Trizol reagent (Quanshijin Company, China), followed by reverse transcription to synthesize complementary DNA. PCR primers were obtained from Shanghai Sangon Biological Engineering Co., Ltd. (China). qRT-PCR reactions were carried out to generate standard curves for each specimen group, and Ct values were processed using computer software. Relative gene expression levels were determined through the $2^{-\Delta\Delta Ct}$ approach, normalized against glyceraldehyde-3-phosphate dehydrogenase. The mRNA expression of inflammatory mediators, encompassing interleukin-6 (IL-6), interleukin-1β (IL-1β), tumor necrosis factor-α (TNF-α), and ATP7A, in HaCaT cells and animal tissues was assessed through qRT-PCR. Primer sequences utilized for qRT-PCR are presented in Table 1.

Western Blot

Western blot was employed to assess ATP7A protein expression in cells and mouse skin tissues. After modeling, samples were homogenized, lysed, and centrifuged, and the resulting supernatants were collected for protein quantification to prepare protein extracts. For each sample, 500 μg of protein was combined with 6× sodium dodecyl sulfate loading buffer at a 5:1 ratio and denatured at 100 °C for 10 min in a metal bath. Subsequently, 60 μg of denatured protein from each

Table 1 The qPCR Primers Used in This Study

Gene Name	Forward Primer (5'->3')	Reverse Primer (5'->3')
TNF-α	CGGGCAGGTCTACTTTGGAG	ACCCTGAGCCATAATCCCCT
IL-1β	AATCTCGCAGCAGCACATCA	GGAAGGTCCACGGGAAAGAC
IL-6	AGACAAAGCCAGAGTCCTTCAG	TGTGACTCCAGCTTATCTCTTGG
GAPDH	AACTTTGGCATTGTGGAAGGG	GACACATTGGGGGTAGGAACA
ATP7A	GTCTCTGGGATGACCTGTGC	TTCCCCAGCGTTTTCCATCA

sample underwent separation and transfer onto membranes. After transferring, the membranes underwent a rinse in Tris-Buffered Saline containing Tween-20 (TBST) for 10 min, followed by a blocking step using 5% non-fat milk at ambient temperature for 1 h. The membranes subsequently experienced three TBST washing cycles (10 min per cycle) and were subjected to overnight exposure at 4 °C with primary antibodies at a 1:1,000 dilution. After three additional TBST cleansing procedures, secondary antibodies diluted to 1:10,000 in blocking solution were introduced and maintained at room temperature for 1 h. Membranes again received three washes with TBST, underwent exposure to chemiluminescent substrate for 1 min, and received visualization using an exposure instrument. ImageJ software is used for image processing and densitometric analysis. Relative protein expression was calculated as the ratio of the gray value of the target protein to that of the internal reference protein.

Statistical Analysis

Statistical analyses were executed employing GraphPad Prism 7 software. Following verification of normal distribution (Shapiro–Wilk test) and homogeneity of variance (Brown–Forsythe test), results were expressed as arithmetic mean ± standard error of the mean. Two-tailed t tests (with Welch's correction) compared 2 groups.The significance levels are as follows: *P < 0.05, **P < 0.01, ***P < 0.001.

Results

Bioinformatics Analysis Results

Screening of Gene Microarray Datasets Meeting Inclusion Criteria

According to the predefined screening standards, a single eligible gene microarray dataset, GSE41078, was identified. This dataset consisted of skin-derived gene profiles and included 20 samples in total, comprising 10 from photodamaged lesions and 10 from normal skin controls.

DEGs of Photodamage

From dataset GSE41078, DEGs between normal and photodamaged samples were identified employing the R package limma, and the results were visualized by volcano plots and heatmaps (Figure 2). A total of 509 DEGs were detected, of which 290 were upregulated and 219 were downregulated.

Functional Enrichment Analysis of DEGs

GO and KEGG enrichment analyses were conducted in R to investigate the biological significance of the identified DEGs. As depicted in (Figure 3A and B), GO analysis demonstrated that DEGs were enriched across the categories of biological processes (BP), cellular components (CC), and molecular functions (MF). For BP, UVB primarily influenced cellular chemotaxis, leukocyte migration, oxidative stress response, and copper ion response. Within CC, significant enrichment was observed in collagen-containing extracellular matrix, secretory granule lumen, endoplasmic reticulum

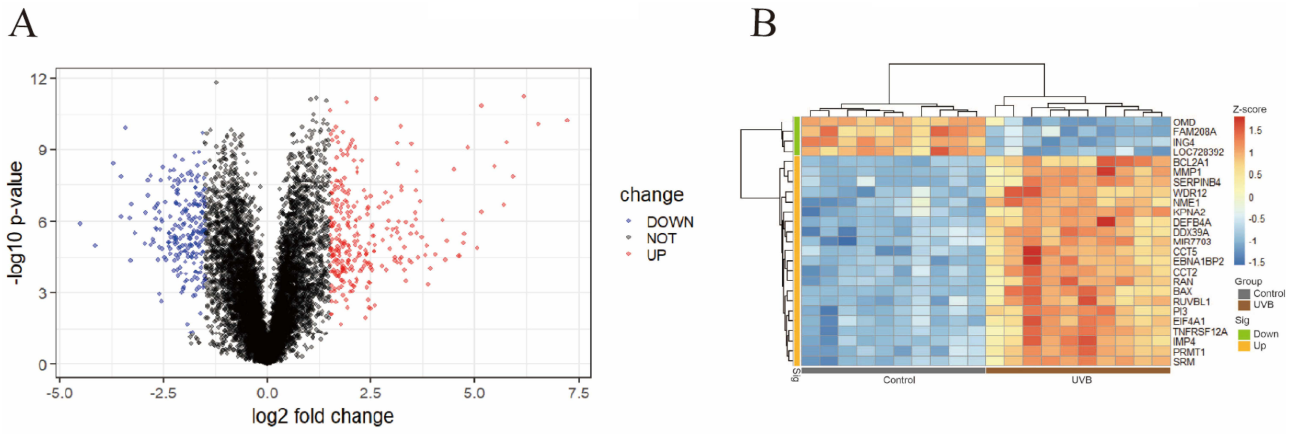

Figure 2 DEGs between UVB-irradiated and non-irradiated tissues. (**A**) Volcano plot of DEGs. (**B**) Heatmap of DEGs.

 https://doi.org/10.2147/CCID.S607933

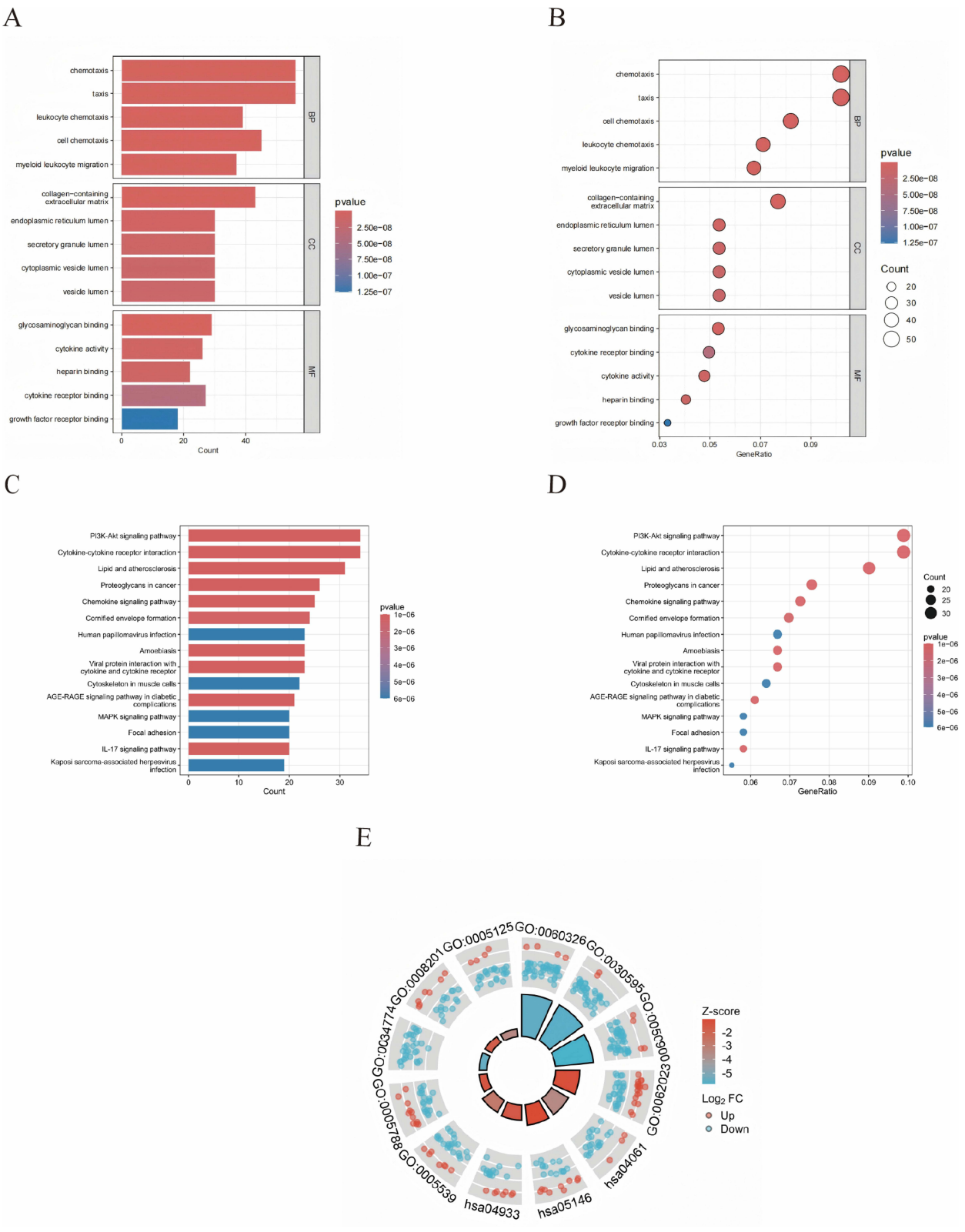

Figure 3 Functional enrichment analysis of DEGs. GO analysis classified the differentially expressed DEGs into three groups (molecular functions, biological processes, and cellular components); (**A**) A bar chart of the differentially expressed DEGs significantly enriched Go terms; (**B**) A bubble plot of the differentially expressed DEGs significantly enriched Go Terms. KEGG analysis of the differentially expressed DEGs; (**C**) A bar chart of the significant pathways of the differentially expressed DEGs; (**D**) A bubble plots of the significant pathways of the differentially expressed DEGs; (**E**) A circle graph of GO functional enrichment and KEGG pathways of DEGs.

https://doi.org/10.2147/CCID.S607933

lumen, and cytoplasmic vesicle lumen. Regarding MF, notable associations were identified with glycosaminoglycan binding, cytokine activity, oxidoreductase activity, and copper ion binding. KEGG pathway analysis additionally revealed that DEGs were predominantly enriched in "cytokine-cytokine receptor interaction", "PI3K-Akt signaling pathway", "glutathione metabolism", and "NF-κB signaling pathway" (Figure 3C–E).

WGCNA Reveals Co-Expression Gene Modules Closely Associated with Photodamage

Sample clustering was conducted using the "WGCNA" package. With a scale-free topology fitting index of 0.9, the soft threshold was set at 12, yielding relatively high average node connectivity (Figure 4A). Six modules were identified through the dynamic tree-cutting algorithm, among which the blue module ($r = –0.91$, $P = 4\times10^{-8}$) exhibited the strongest association with photodamage and comprised 978 hub genes (Figure 4B). Intersecting these 978 hub genes with 55 CRGs and 509 DEGs produced a single key gene (Figure 4C).

Keratinocyte ATP7A Expression Level Correlates with Enhanced Integration of ECM-Adhesion Signaling Networks

ATP7A expression was significantly altered following UVB exposure, with keratinocytes from the UVB group exhibiting markedly lower ATP7A expression compared with Control cells ($p = 1.83\times10-5$). UMAP visualization demonstrated that ATP7A expression was broadly distributed across the keratinocyte population rather than confined to a discrete subcluster, indicating a condition-associated transcriptional shift rather than the emergence of a rare cell state. On this basis, keratinocytes were stratified into ATP7Ahigh and ATP7Alow subpopulations for subsequent cell–cell communication analysis. CellChat in ference revealed a dense intercellular communication network dominated by stromal–epithelial interactions, with fibroblasts and endothelial cells acting as major signaling hubs. Although both keratinocyte subpopulations were centrally positioned within the network, ATP7Ahigh keratinocytes exhibited stronger integration, particularly in interactions involving stromal and structural cell types. Ligand–receptor pair analysis further demonstrated that extracellular matrix and adhesion-related signaling constituted the predominant communication axis targeting keratinocytes, including collagen–receptor (eg., COL1A1/1A2/4A1/6A1–CD44/SDC1/SDC4), laminin–receptor (LAMA/LAMB/LAMC–CD44/DAG1), fibronectin-mediated adhesion (FN1–integrin/CD44), and thrombospondin- and tenascin-associated interactions engaging CD47 and syndecans. These ECM-driven signals were consistently stronger toward ATP7Ahigh keratinocytes, suggesting that UVB-associated ATP7A downregulation is coupled to weaken responsiveness to microenvironmental structural and adhesion cues, whereas immune-related signaling differences were comparatively modest (Figure 5).

In vitro Experimental Validation Results

H&E Staining of Mouse Skin Tissue

In comparison with the control group, histopathological analysis of the UVB group demonstrated a thickened stratum corneum, hyperkeratosis, and lymphocyte-dominant inflammatory infiltration within the superficial and middle dermal layers following UVB exposure (Figure 6).

Relative mRNA Expression Levels of Inflammatory Factors in UVB-Induced Photodamage Cell and Mouse Models

In the UVB cell model, IL-1β expression was markedly elevated ($P < 0.05$), while IL-6 and TNF-α showed highly significant upregulation ($P < 0.01$) versus the control group. In the UVB mouse model, IL-6 expression increased markedly ($P < 0.05$), and both IL-1β and TNF-α exhibited highly significant increases ($P < 0.01$), confirming that UVB effectively established photodamage in cell and animal models (Figure 7).

mRNA and Protein Levels of ATP7A in Photodamaged Cells and Animal Models

qRT-PCR analysis suggested that ATP7A mRNA expression was markedly downregulated in UVB-treated cells and animal models compared with the control groups ($P < 0.05$). WB analysis further confirmed that ATP7A protein expression was also markedly reduced in both photodamaged cells and animal tissues (all $P < 0.05$). These findings

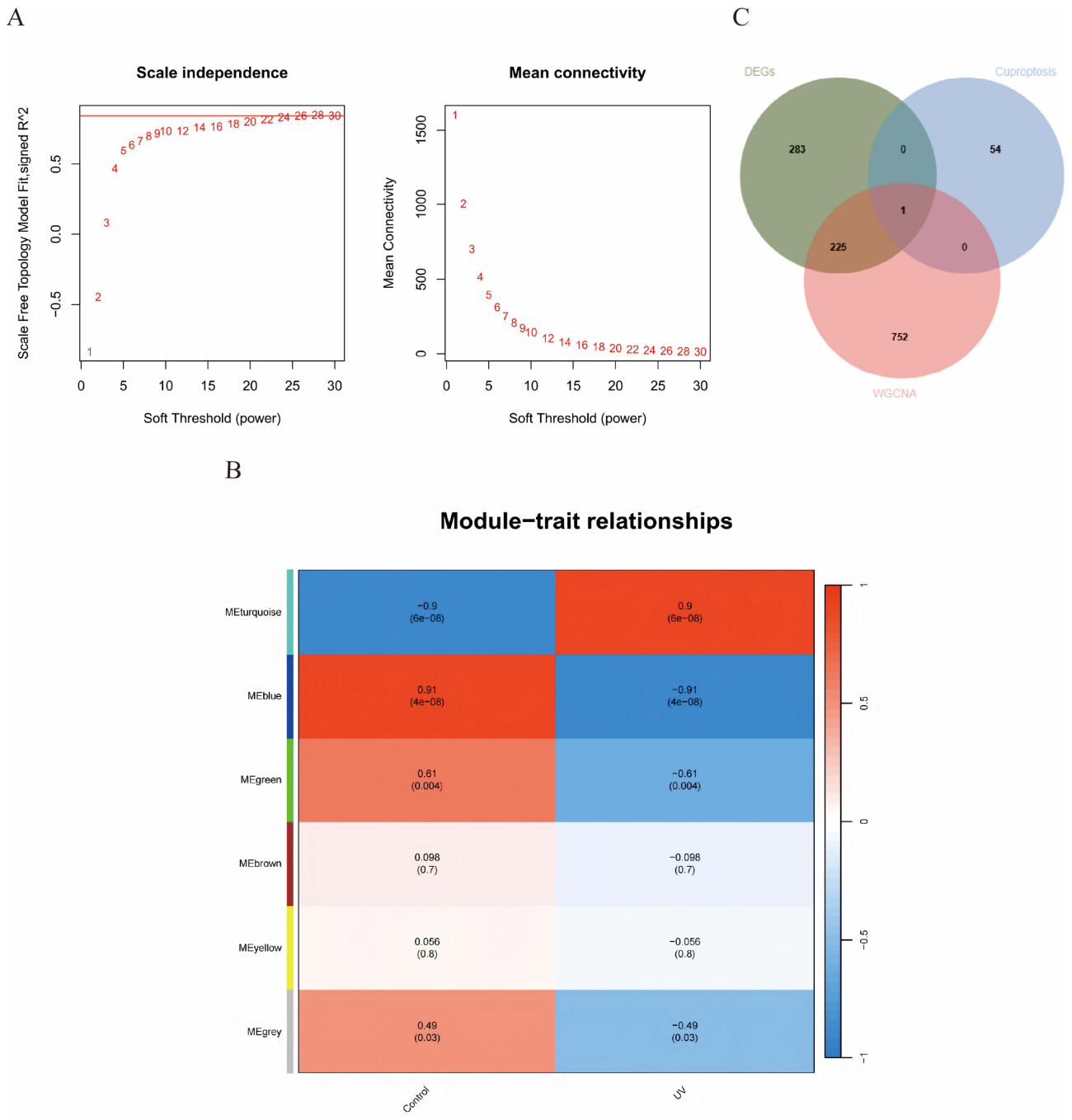

Figure 4 Weighted gene co-expression network analysis. (**A**) Selection of the optimal soft threshold power. (**B**) Heatmap of module-trait relationships showing the correlations between identified gene modules and experimental conditions. (**C**) Venn diagram showing the intersection of 978 hub module genes from the blue module with 55 CRGs and 509 DEGs.

suggest that UVB-induced photodamage suppresses ATP7A expression, consistent with the predictions from prior bioinformatics analysis (Figure 8).

Discussion

Photodamage refers to the acute responses triggered by UV exposure, such as sunburn and inflammation, whereas chronic UV-induced injury contributes to skin aging,[24] a condition inevitably encountered with time. Prolonged UV radiation generates excessive ROS, disrupting the intracellular redox balance, impairing antioxidant enzyme activity, and

https://doi.org/10.2147/CCID.S607933

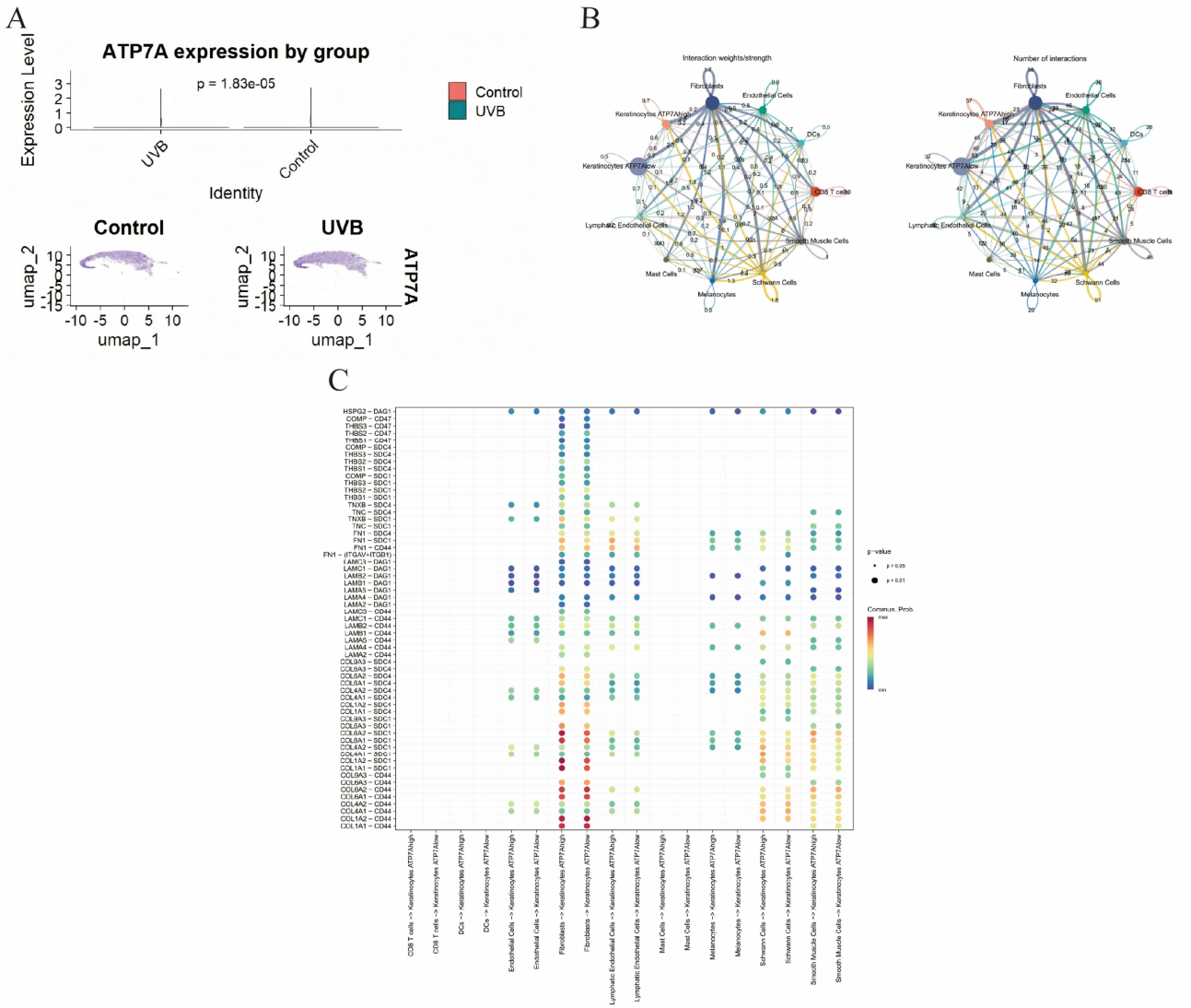

Figure 5 (**A**) Violin plot showing ATP7A expression levels in keratinocytes from Control and UVB samples. (**B**) Cell-cell communication analysis between keratinocytes with high and low ATP7A expression. (**C**) Ligand–receptor pair analysis demonstrates that ECM and adhesion-related signaling constitutes the predominant communication axis targeting keratinocytes.

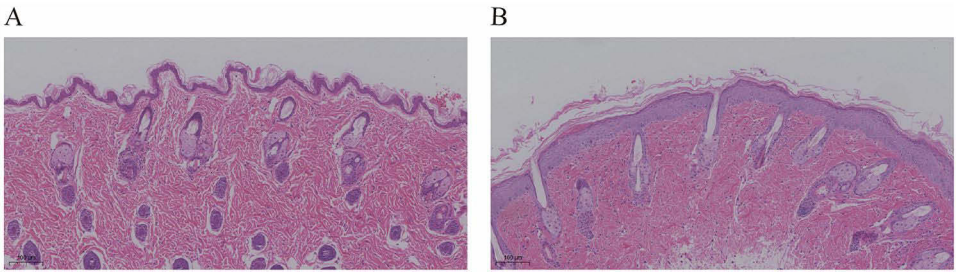

Figure 6 Histopathological manifestations of mouse skin tissue (H&E staining ×100). (**A**) Control group. (**B**) UVB group.

producing large quantities of oxygen-free radicals that attack cellular components, thereby initiating oxidative injury characteristic of UVB-induced photodamage.[25] Under sustained UVB exposure, the skin develops classical aging features, including dryness, wrinkling, and abnormal pigmentation.[26] Therefore, elucidating the pathogenic mechanisms of photodamage, identifying molecular targets, and developing preventive strategies are essential for delaying skin aging,

 https://doi.org/10.2147/CCID.S607933

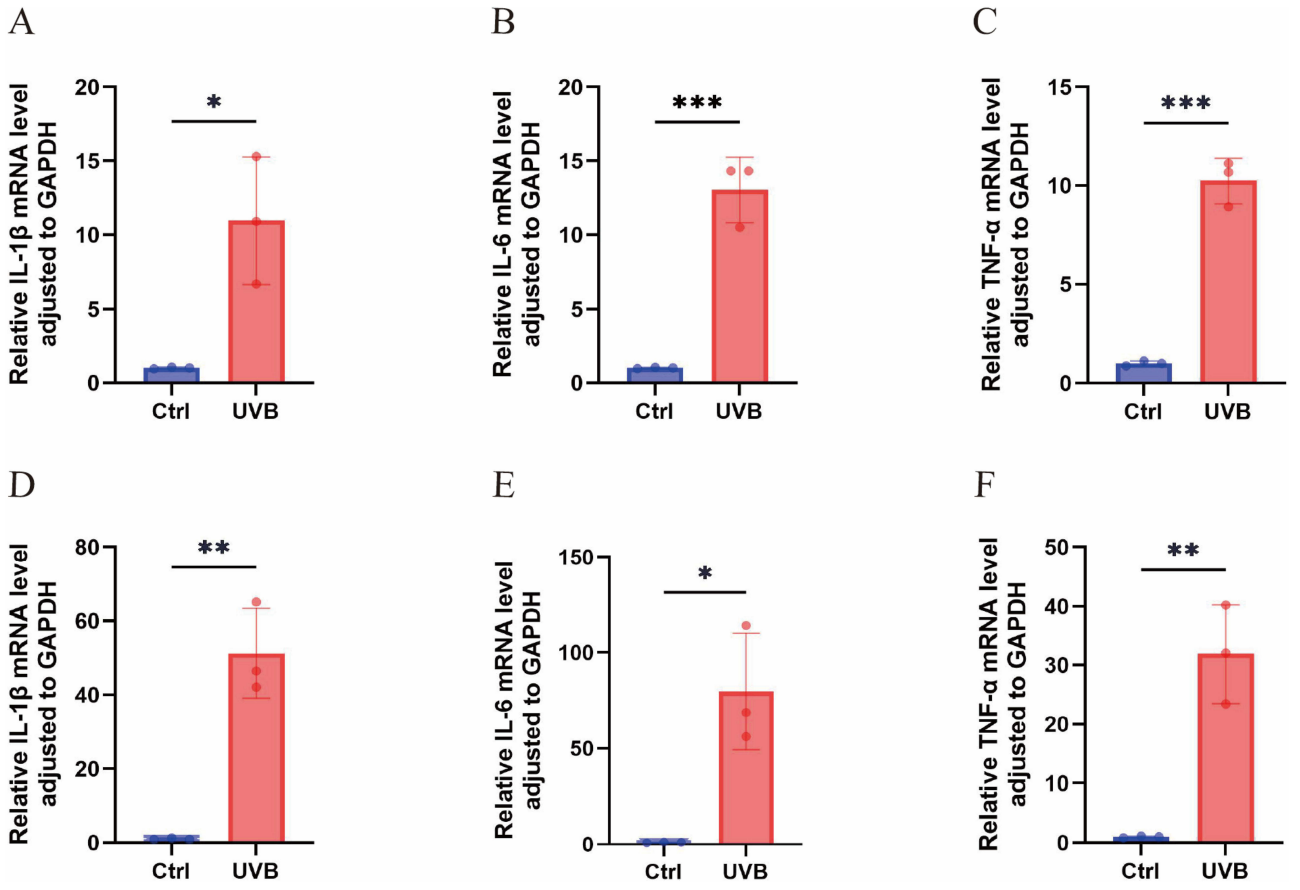

Figure 7 Expression of inflammatory factors in UVB-induced photodamage in cell and mouse models. (**A**) Relative mRNA expression of IL-1β in the cell models. (**B**) Relative mRNA expression of IL-6 in the cell models. (**C**) Relative mRNA expression of TNF-α in the cell models. (**D**) Relative mRNA expression of IL-1β in the animal models. (**E**) Relative mRNA expression of IL-6 in the animal models. (**F**) Relative mRNA expression of TNF-α in the animal models. Data are shown as mean ± SEM (*P < 0.05; **P < 0.01; ***P < 0.001).

carcinogenesis, and other age-related dermatological disorders. Currently, no study has addressed the relationship between photodamage and cuproptosis. With advances in gene sequencing and bioinformatics methodologies, extensive sequencing datasets have become available. Therefore, bioinformatics methodologies were employed to investigate the molecular mechanisms and potential targets of UVB-induced photodamage. The results indicated that UVB-induced photodamage is strongly associated with cuproptosis, a finding that may provide novel biomarkers and deepen understanding of its pathogenic processes.

Copper, a redox-active metal ion,[27] supports mitochondrial oxidative phosphorylation, energy production, redox equilibrium, and extracellular matrix remodeling in skin tissue[28], collagen and melanin synthesis.[29] Under physiological conditions, intracellular copper levels are coordinately regulated by a protein network consisting of copper-dependent enzymes, copper chaperones, and membrane transporters, which control influx, efflux, and intracellular distribution. Divalent copper (Cu^{2+}) enters cells via the six-transmembrane epithelial antigen of prostate and copper transporter 1 (CTR1), where it is reduced to monovalent copper (Cu^{+}). Cu^{+} is then distributed to subcellular compartments to fulfill its biological roles, while excess Cu+ is exported through ATP7A and copper-transporting ATPase β (ATP7B) at the plasma membrane to preserve homeostasis.[30] Once inside the cell, copper can be sequestered by metallothionein or bound to copper chaperones, including copper chaperone for superoxide dismutase, cytochrome C oxidase 17, and antioxidant protein 1, for targeted delivery to subcellular organelles, where it exerts antioxidant activity.[31] Within mitochondria, metabolic enzymes such as cytochrome C oxidase and superoxide dismutase 1 serve as essential components for neutralizing free radicals and mitigating oxidative stress.[32–36] Furthermore, aided by antioxidant protein 1, copper is

https://doi.org/10.2147/CCID.S607933

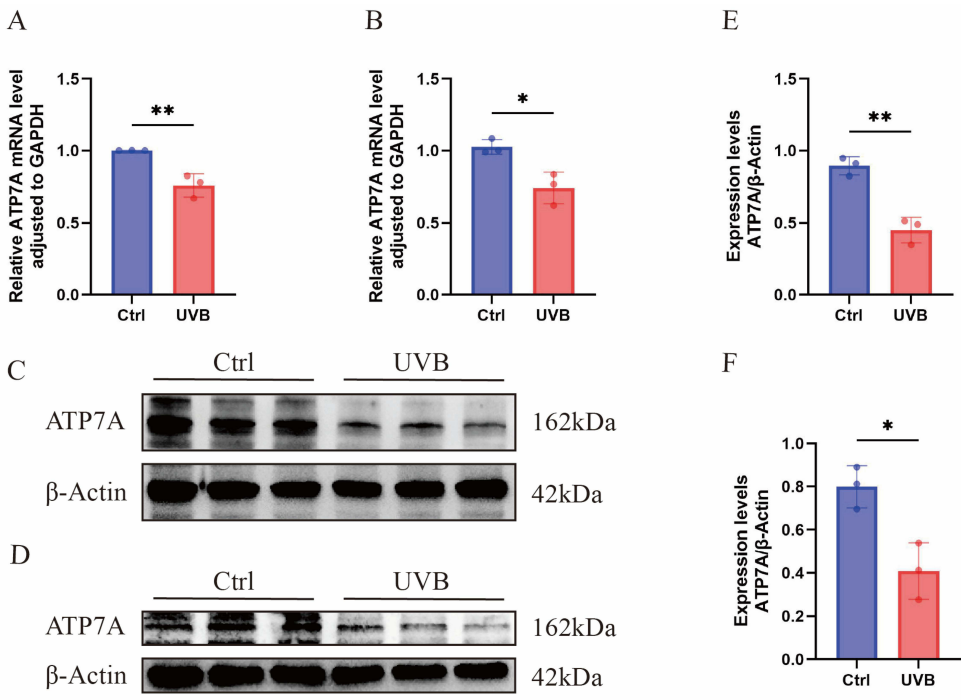

Figure 8 Expression of ATP7A mRNA and protein levels in UVB-induced photodamaged cell and mouse models. (**A**) Relative mRNA expression of ATP7A in the cell models. (**B**) Relative mRNA expression of ATP7A in the mouse models. (**C**) Protein expression levels of ATP7A in the cell models were detected by WB, respectively. (**D**) Protein expression levels of ATP7A in the mouse models were detected by WB, respectively. (**E**) Comparison of ATP7A protein expression between control and UVB groups in the cell models, respectively. (**F**) Comparison of ATP7A protein expression between control and UVB groups in the mouse models, respectively. Data are shown as mean ± SEM (*$P < 0.05$; **$P < 0.01$).

directed to ATP7A and ATP7B in the trans-Golgi network, where it enters the lumen and associates with copper-dependent enzymes,[37] thereby ensuring proper Golgi apparatus function.

Cuproptosis represents a unique mode of cell death induced by excessive copper accumulation, occurring when copper ionophores such as elesclomol and disulfiram transport copper into cells.[13] Through experimental screening, Tsvetkov et al[11] identified elesclomol as a copper ionophore and demonstrated that cuproptosis proceeds via a set of regulatable effector pathways. Cells relying on mitochondrial respiration were found to be highly sensitive to copper-loaded elesclomol. Once copper enters mitochondria, it does not directly affect the electron transport chain. Conversely, under the regulation of ferredoxin 1, it promotes acylated protein oligomerization, thereby redirecting associated enzymes into the tricarboxylic acid cycle, disrupting metabolism, and ultimately inducing cell death.

Based on bioinformatics analysis of the GSE41078 dataset from the GEO database, 509 photodamage-associated DEGs were identified, encompassing 290 upregulated and 219 downregulated genes. Functional enrichment analyses (GO and KEGG) and WGCNA were subsequently applied to these DEGs. Moreover, CRGs were procured from the Genecards database, and the overlap among DEGs, WGCNA modules, and CRGs was examined. ATP7A was ultimately recognized as a hub gene linked to cuproptosis in photodamage, with expression markedly downregulated. Literature review further indicated that ATP7A shows a consistent downregulation trend during cuproptosis, aligning with expression changes detected in photodamage. To validate these observations, UVB-induced photodamage models were established in both cells and animals. Experimental results revealed that ATP7A expression at both mRNA and protein levels was markedly reduced compared with controls in both models, consistent with the bioinformatics findings. Collectively, these results suggest that alterations in cuproptosis may occur during UVB-induced photodamage.

ATP7A is a copper-transporting P-type ATPase that contains six N-terminal copper-binding motifs and a catalytic transduction core with multiple functional domains[38], and is expressed in nearly all tissues except the liver. Under physiological conditions, ATP7A cooperates with CTR1 to regulate intracellular and extracellular copper homeostasis.[39] Previous investigations have primarily linked ATP7A to hereditary disorders, particularly Menkes disease, an X-linked

recessive neurodegenerative condition resulting from defective copper metabolism.[40] In the context of photodamage, UVB exposure may compromise ATP7A function. Normally, ATP7A mediates the transport of excess intracellular copper either to the Golgi apparatus or across the plasma membrane. However, functional impairment may lead to altered intracellular copper distribution, although this requires further experimental validation. This abnormal copper retention is regarded as a major mechanism underlying cuproptosis. Moreover, accumulated Cu^{+} can catalyze the conversion of hydrogen peroxide (H_2O_2) into highly reactive hydroxyl radicals via Fenton-like reactions, markedly increasing intracellular ROS levels. Excessive ROS induces extensive cellular injury, including DNA damage, mitochondrial dysfunction, and loss of membrane integrity,[41] Collectively, these effects exacerbate oxidative stress and may be associated with apoptotic signaling.[13] It is noteworthy that the mechanism by which copper ions induce ROS production and exert cytotoxic effects has been extensively explored in cancer research. For instance, the copper ion carrier NSC319726 promotes ROS generation by activating Cu^{2+}, thereby inhibiting DNA synthesis and leading to G1-phase cell cycle arrest and cell death.[42] Additionally, disulfiram promotes reactive oxygen species (ROS) production upon binding to Cu^{2+}, inducing tumor cell death by activating the p38 signaling pathway and inhibiting the nuclear factor κB (NF-κB) signaling pathway.[43] Based on the aforementioned mechanism, in normal skin cells, UVB exposure causes copper accumulation and ROS bursts by damaging ATP7A, suggesting that a copper-induced death mechanism may also exist. This indicates a close correlation between photodamage and copper-induced cell death.

This study has several limitations. First, the bioinformatics analysis relies solely on a single public dataset, which may affect the generalizability and robustness of the results. Second, the animal experiments were performed with a relatively small sample size, which may limit the statistical power and reproducibility of the findings. Third, the experimental validation is primarily restricted to expression-level analyses (qRT-PCR and Western blot), without functional assays (eg., gene knockdown/overexpression, rescue experiments, or pathway interventions) to directly test the proposed biological mechanisms.

Conclusions

In summary, this study suggests that ATP7A, a copper transporter, may be associated with oxidative stress responses in UVB-induced skin photodamage, based on integrated bioinformatic analyses and preliminary validation in cellular and animal models using qRT-PCR and WB. The findings also indicate that copper death may be associated with UVB-induced photodamage, with ATP7A potentially contributing to ECM-adhesion signaling dysfunction. While these results identify ATP7A as a candidate for further functional studies, additional experiments are required to establish its precise role and therapeutic relevance.

Ethics Approval and Consent to Participate

In accordance with the "Ethical Review Measures for Life Science and Medical Research Involving Humans" (issued on February 18, 2023, by the People's Republic of China), this study complies with Article 32, Items 1 and 2, and falls under the category of research that does not require ethical review. The relevant provisions are as follows:

Article 32, Item 1: Research that does not involve human samples, data, or personal privacy, and where there is no direct intervention or collection of sensitive information from individuals, does not require ethical approval.

Article 32, Item 2: Research conducted using publicly available anonymized data or de-identified biological samples, and where no new interventions are made on participants, does not require ethical approval.

Therefore, this study does not require ethical review approval.

Author Contributions

All authors made a significant contribution to the work reported, whether that is in the conception, study design, execution, acquisition of data, analysis and interpretation, or in all these areas; took part in drafting, revising or critically reviewing the article; gave final approval of the version to be published; have agreed on the journal to which the article has been submitted; and agree to be accountable for all aspects of the work.

Funding

Project funded by the National Natural Science Foundation of China((No.82460621).

Disclosure

The authors declare no conflicts of interest in this work.

References

1. Harris-Tryon A, Grice EA. Microbiota and maintenance of skin barrier function. *Science*. 2022;376(6596):940–945. doi:10.1126/science.abo0693
2. Mariáurea MS, Reggiani VG, Giuseppe V. Cutaneous redox senescence. *Biomedicines*. 2024;12. doi:10.3390/biomedicines12020348
3. Wilson SR, Madronich S, Longstreth JD, et al. Interactive effects of changing stratospheric ozone and climate on tropospheric composition and air quality, and the consequences for human and ecosystem health. *Photochem Photobiol Sci*. 2019;18(3):775–803. doi:10.1039/c8pp90064g
4. Bianca OS, Rayssa LM, Fonseca A, et al. An ex vivo model of human skin photoaging induced by UVA radiation compatible with summer exposure in Brazil. *J Photochem Photobiol B*. 2021;221:112–125. doi:10.1016/j.jphotobiol.2021.112255
5. Zahra R, Alireza A. Examination of the biological effects of sunlight on the skin: a review. *J Lasers Med Sci*. 2026;16. doi:10.34172/jlms.2025.52
6. Afnan Q, Kaiser PJ, Rafiq RA, et al. Glycyrrhizic acid prevents ultraviolet-B-induced photodamage: a role for mitogen-activated protein kinases, nuclear factor kappa B and mitochondrial apoptotic pathway. *Exp Dermatol*. 2016;25(6):440–446. doi:10.1111/exd.12964
7. Kim B-H, Choi MS, Lee HG, et al. Photoprotective potential of penta-O-Galloyl-β-DGlucose by targeting NF-κB and MAPK signaling in UVB radiation-induced human dermal fibroblasts and mouse skin. *Mol Cells*. 2015;38(11):982–990. doi:10.14348/molcells.2015.0169
8. Scharffetter KK, Wlaschek DM, Harris A, et al. UV-induced reactive oxygen species in photocarcinogenesis and photoaging. *Biol Chem*. 1998;378:247–257. doi:10.1111/j.1467-2494.1995.tb00118.x
9. He H, Xiong L, Jian L, et al. Role of mitochondria on UV-induced skin damage and molecular mechanisms of active chemical compounds targeting mitochondria. *J Photochem Photobiol B*. 2022;232:112–124. doi:10.1016/j.jphotobiol.2022.112464
10. Malik AT, Haroon R, Sheikh AT. Molecular basis of skin photoaging and therapeutic interventions by plant-derived natural product ingredients: a comprehensive review. *Heliyon*. 2023;9. doi:10.1016/j.heliyon.2023.e13580
11. Wang Z, Li A, Huang X, et al. HSP27 protects skin from ultraviolet B -induced photodamage by regulating autophagy and reactive oxygen species production. *Front Cell Dev Biol*. 2022;10:222–244. doi:10.3389/fcell.2022.852244
12. Deng L, Li Y, Wu Q, et al. Investigating potential ferroptosis-related differentially expressed genes of UVB-induced skin photodamage. *Int J Dermatol*. 2022;62(1):79–87. doi:10.1111/ijd.16472
13. Tsvetkov P, Coy S, Petrova B, et al. Copper induces cell death by targeting lipoylated TCA cycle proteins. *Science*. 2022;375(6586):1254–1261. doi:10.1126/science.abf0529
14. Wang J, Chen Z, Shang H, et al. The molecular mechanisms of cuproptosis and its relevance to atherosclerosis. *Biomole Biomed*. 2025;25 (8):1709–1722. doi:10.17305/bb.2024.11826
15. Scot CL, Dennis RW. The Janus face of copper: its expanding roles in biology and the pathophysiology of disease. Meeting on copper and related metals in biology. *EMBO Rep*. 2007;8(3):224–227. doi:10.1038/sj.embor.7400915
16. Zhu Z, Song M, Ren J. Copper homeostasis and cuproptosis in central nervous system diseases. *Cell Death Dis*. 2024;15(1):15. doi:10.1038/s41419-024-07206-3
17. Shen Z, Liu Z, Cai S, et al. Copper homeostasis and cuproptosis in myocardial infarction: molecular mechanisms, treatment strategies and potential therapeutic targets. *Front Pharmacol*. 2025;16. doi:10.3389/fphar.2025.1525585
18. Huang X, Shen J, Huang K, et al. Cuproptosis in cancers: function and implications from bench to bedside. *Biomed Pharmacother*. 2024;176. doi:10.1016/j.biopha.2024.116874
19. Ashburner M, Ball C, Blake J, et al. Gene ontology: tool for the unification of biology. *Gene Ontol Consortium Nat Genet*. 2000;25:25–39. doi:10.1038/75556
20. Altermann E, Klaenhammer TR. PathwayVoyager: pathway mapping using the Kyoto Encyclopedia of Genes and Genomes (KEGG) data-base {J.2005;6:60. *BMC Genomies*. 2005;6:112~128. doi:10.1038/s41598-025-17722-7
21. Yu G, Wang L, Han Y, et al. clusterProfiler: an R package for comparing biological themes among gene clusters. *OMICS*. 2012;16(5):284–287. doi:10.1089/omi.2011.0118
22. Khwandow K, Wattanased J, Linda C, et al. Potential use of amla (*Phyllanthus emblica* L.) fruit extract to protect skin keratinocytes from inflammation and apoptosis after UVB Irradiation. *Antioxidants*. 2021;10. doi:10.3390/antiox10050703
23. Park G, Qian W, Zhang M-J, et al. Platelet-rich plasma regulating the repair of ultraviolet B–induced acute tissue inflammation: adjusting macrophage polarization through the activin receptor–follistatin system. *Bioengineered*. 2021;12(1):3125–3136. doi:10.1080/21655979.2021.1944026
24. TzuYu L, PoYuan W, ChienWei H, et al. Protective effects of sesamin against UVB-induced skin inflammation and photodamage in vitro and in vivo. *Biomolecules*. 2019;9:909–929. doi:10.3390/biom9090479
25. Wang S, Yang M, Yin S, et al. A new peptide originated from amphibian skin alleviates the ultraviolet B-induced skin photodamage. *Biomed Pharmacother*. 2022;150:112987. doi:10.1016/j.biopha.2022.112987
26. Peng Z, Chen B, Zheng Q, et al. Ameliorative effects of peptides from the oyster (crassostrea hongkongensis) protein hydrolysates against UVB-induced skin photodamage in mice. *Mar Drugs*. 2020;18(6):288. doi:10.3390/md18060288
27. Kim BE, Nevitt T, Thiele DJ. Mechanisms for copper acquisition, distribution and regulation. *Nat Chem Biol*. 2008;4(3):176–185. doi:10.1038/nchembio.72
28. Yang Y, Qi F, Ying L, et al. Exploring cuproptosis as a mechanism and potential intervention target in cardiovascular diseases. *Front Pharmacol*. 2023;14:1042–1057. doi:10.3389/fphar.2023.1229297
29. Tsang T, Davis CI, Brady DC. Copper biology. *Curr Biol*. 2021;31(9):R421–R427. doi:10.1016/j.cub.2021.03.054
30. Stefanie DB, Morgan SU, Amelie S, et al. Copper sources for sod1 activation. *Antioxidants*. 2020;9:37–55. doi:10.3390/antiox9060500
31. Linder M, Hazegh-Azam M. Copper biochemistry and molecular biology. *Am J Clin Nutr*. 1996;63(5):797S–811S. doi:10.1093/ajcn/63.5.797
32. Payan-Carreira R, Santos C, Santos D. Antioxidant enzyme dynamics suggest the absence of oxidative stress in the canine endometrium across the estrous cycle. *Anim Reprod Sci*. 2025;275. doi:10.1016/j.anireprosci.2025.107819

33. Zischka H, Einer C. Mitochondrial copper homeostasis and its derailment in Wilson disease. *Int J Biochem Cell Biol*. 2018;102:71–75. doi:10.1016/j.biocel.2018.07.001
34. PetruIulian T, Marcel U, Bahia K, et al. Cooperation between two periplasmic copper chaperones is required for full activity of the cbb 3 -type cytochrome c oxidase and copper homeostasis in Rhodobacter capsulatus. *Mol Microbiol*. 2016;100(2):345–361. doi:10.1111/mmi.13321
35. Kawamata H, Manfredi G. Import, maturation, and function of SOD1 and its copper chaperone CCS in the mitochondrial intermembrane space. *Antioxid Redox Signal*. 2010;13(9):1375–1384. doi:10.1089/ars.2010.3212
36. Blockhuys S, Celauro E, Hildesjö C, et al. Defining the human copper proteome and analysis of its expression variation in cancers. *Metallomics*. 2016;9(2):112–123. doi:10.1039/c6mt00202a
37. Baker ZN, Cobine PA, Leary SC. The mitochondrion: a central architect of copper homeostasis. *Metallomics*. 2017;9(11):1501–1512. doi:10.1039/c7mt00221a
38. Chen J, Jiang Y, Shi H, et al. The molecular mechanisms of copper metabolism and its roles in human diseases. *Pflugers Arch*. 2020;472(10):1415–1429. doi:10.1007/s00424-020-02412-2
39. Hiroko K, Chie F, Wattanaporn B. Inherited copper transport disorders: biochemical mechanisms, diagnosis, and treatment. *Curr Drug Metab*. 2011;13:237–250. doi:10.2174/138920012799320455
40. De Feyter S, Beyens A, Callewaert B. ATP7A-related copper transport disorders: a systematic review and definition of the clinical subtypes. *J Inherit Metab Dis*. 2023;46(2):163–173. doi:10.1002/jimd.12590
41. Gan Y, Liu T, Feng W, et al. Drug repositioning of disulfiram induces endometrioid epithelial ovarian cancer cell death via the both apoptosis and cuproptosis pathways. *Oncol Res*. 2023;31(3):333–343. doi:10.32604/or.2023.028694
42. Shimada K, Reznik E, Stokes ME, et al. Copper-binding small molecule induces oxidative stress and cell-cycle arrest in glioblastoma-patient-derived cells. *Cell Chem Biol*. 2018;25(5):585–594. doi:10.1016/j.chembiol.2018.02.010
43. Ren X, Li Y, Zhou Y, et al. Overcoming the compensatory elevation of NRF2 renders hepatocellular carcinoma cells more vulnerable to disulfiram/copper-induced ferroptosis. *Redox Biol*. 2021;46:102–122. doi:10.1016/j.redox.2021.102122